



Electronic modulation induced by oxygen vacancy creating in copper oxides toward accelerated hydrogenation kinetics of nitroaromatics

Longlong Geng ^{a,1}, Qing Zhang ^{a,1}, Xiaoli Wang ^{a,*}, Haixiang Han ^b, Yong-Zheng Zhang ^{a,*}, Chunhui Li ^a, Zhen Li ^a, Da-Shuai Zhang ^a, Xiuling Zhang ^a, Abdulkader Abdulkayum ^c, Guangzhi Hu ^{d,*}

^a Shandong Provincial Key Laboratory of Monocrystalline Silicon Semiconductor Materials and Technology, College of Chemistry and Chemical Engineering, Dezhou University, Dezhou 253023, China

^b School of Materials Science and Engineering, Tongji University, Shanghai 201804, China

^c Xinjiang Key Laboratory of Novel Functional Materials Chemistry, College of Chemistry and Environmental Sciences, Kashi University, Kashi 844000, China

^d Institute for Ecological Research and Pollution Control of Plateau Lakes, School of Ecology and Environmental Science, Yunnan University, Kunming 650504, China



ARTICLE INFO

Keywords:

Heterogeneous catalysis, oxygen vacancy
Copper oxide
Catalytic reduction
4-nitrophenol

ABSTRACT

The development of advanced catalysts is of vital importance for chemical production, and vacancy engineering represents an effective approach to improve the overall catalytic activities by modulating their structural characters. Herein, a series of oxygen-vacancy-functionalized copper oxides were effectively prepared through a hydrothermal-oxidative tandem process. The optimized CuO-S30 catalyst shows an exceptionally-improved catalytic performance for the selective hydrogenation of 4-nitrophenol (4-NP) with good reusability. With the assistance of theoretical simulation, the exceptional activity can be attributed to the electronic modulation induced by oxygen vacancies in CuO-S30, which could not only facilitate the trapping of the reactants on the positively charged Cu sites, but also promote the electron transfer during the hydrogenation process. This study offers a facile and environmentally friendly strategy for electronic property modulation in metal oxides by oxygen vacancies construction, which can be further extended to other advanced catalysts with outstanding catalytic properties.

1. Introduction

Chemical production is an important activity in human production and life, in particular, about 90 % of chemical production requires the participation of catalysts. Currently, most industrial catalysts exist in the form of blocks, therefore only the surface metal species are involved in catalytic reactions, resulting in low catalyst utilization and inferior catalytic activity [1–5]. With the development of nanotechnology, further improvement of catalyst utilization and catalytic properties becomes probable through the development of advanced metal-based catalysts in micron or even nanoscale. For example, nanoparticles composed of metal or alloys can be obtained by wet reduction measures, or supported metal clusters or even single-atom catalysts can be prepared using biochar, boron nitride, and metal oxides as supports [6–11]. So far, some successes have been achieved in design and preparation of versatile catalysts in the laboratory, which also show satisfactory

catalytic behaviors from the perspective of industrial applications [12–15]. However, additional engineering process need to be introduced, such as heteroatom doping and vacancy defect modulation, to develop better-performing catalysts in specific areas and facilitate the production of fine chemicals.

The epidemic situation caused by COVID-19 has caused enormous damage to human health and global security. In particular, the extensive use of paracetamol, a highly effective antipyretic for COVID-19, has resulted in a significant increase in the demand for amino-substituted aromatic compounds [16,17]. Notably, arylamine compounds belong to a family of intermediates in chemical production and are widely used in the fields of printing and dyeing, pharmaceutical research and development, pesticide production, and so on [18–22]. Generally, these compounds could be synthesized via either a non-catalytic route or a catalytic reduction process [23–25]. Metallic metals or acids and toxic organic reagents are usually required in a non-catalytic synthesis

* Corresponding authors.

E-mail addresses: wang52@mail.ustc.edu.cn (X. Wang), zhangyongzheng23@163.com (Y.-Z. Zhang), guangzhihu@ynu.edu.cn (G. Hu).

¹ These authors contributed equally.

process. In comparison to the traditional methods which usually employ strong acids, heat, and high pressures, selective reduction of nitroarenes to synthesize corresponding arylamine compounds in the presence of catalysts and reducing agent is a highly economical and environmentally friendly route [26,27]. Additionally, the conversion of nitroaromatics into value-added amino aromatic compounds is also an important means to promote industrial development, but this process is largely dependent on the development of catalysts. Noble metal-based materials, such as Pt, Pd, and Au, were used as catalysts to promote the hydrogenation of nitroaromatics due to their excellent capability for hydrogen adsorb and activation [28–31]. However, the scarcity and high cost of noble-metal elements limit the large-scale application of these materials. Researchers are turning their attention to more economical non-noble metal materials, such as cobalt-, nickel-, or copper-based materials [32,33]. However, the low activities and kinetics, especially under mild conditions, are the main challenges that urgently need to be addressed for such catalysts.

Recently, it has been proved that introduction of oxygen vacancies in metal oxides through defect engineering could largely improve the catalytic performance of non-noble metal-based catalysts. Benefiting from the presence of oxygen vacancies, electronic properties of the metals that are adjacent to oxygen vacancies will adjust automatically, thus further driving the optimization of electrical properties on the catalyst surface. For example, X. Zhao *et al.* prepared nickel oxide nanoparticles by using metal-doped organic polymers as precursors, and realized the efficient production of aniline compounds due to the abundant surface vacancies [34]. Through vacancy engineering in NiFe-layered double hydroxides and MoO_{3-x} -anchored-MXene, Song *et al.* and Chu's group found that the oxygen vacancy played an indispensable role in substrates activation and electronic transport, thus achieving an exceptional oxygen evolution reaction (OER) and N_2 reduction reaction (NRR) activity [35,36]. Combining the above advances, we concluded that regulating the superficial structure of the catalysts, especially modulating the structural/electronic configurations through oxygen vacancies construction, is a favorable strategy for developing catalysts that are conducive for the reduction of nitroaromatics.

In this study, we report the electronic properties modulation on CuO catalyst by superficial oxygen vacancy (O_v) construction, thereby achieving outstanding kinetic enhancement in nitroaromatics reduction. A facile hydrothermal-oxidation tandem method was used for the fabrication of O_v on the surface of CuO catalysts (CuO-S_x, x represents treating time) using $\text{Cu}_2(\text{OH})_3\text{NO}_3$ as the precursor. Interestingly, structural reconfiguration and subsequent O_v construction were achieved in the final catalysts after a combined ultrasound and hydrogen peroxide treatment with ultra-fast rates and green conditions. The catalytic behavior of nitroaromatics reduction on the CuO-S_x as well as the contrasting CuO catalysts was tested, and the promoting effects of O_v on different catalysts were unfolded considering the reaction parameter, dynamic (kinetic) and thermodynamic (energetic) factors. Besides, systemic structural and spectroscopic measurements and DFT simulations were adopted to survey the reactants adsorption on catalysts and related charge transfers during the reaction process. Our work attempts to broaden the strategies for regulating the catalytic capacity of non-precious metals and furtherly understand the role of O_v in enhancing H activation and hydrogenation reactions.

2. Materials and methods

2.1. Chemicals and catalysts preparation

Copper nitrate trihydrate ($\text{Cu}(\text{NO}_3)_2 \cdot 3\text{H}_2\text{O}$), Hexamethylenetetramine (HMTA), sodium hydroxide (NaOH), sodium borohydride (NaBH₄) were purchased from Sinopharm Chemical Reagent. Other organic chemicals and substrates were obtained from Aladdin biochemical Technology and used without further purification.

The $\text{Cu}_2(\text{OH})_3\text{NO}_3$ precursors were prepared by a solvothermal method using copper nitrate trihydrate as metal source and sodium hydroxide and hexamethylenetetramine as alkaline precipitators (more synthesis details see Experimental Section in [Supporting information](#)). For the synthesis of CuO-S30, 0.5 g of the above precursor was added to 30 mL of hydrogen peroxide solution (30 %) and reacted for 30 min under sonication conditions, followed by centrifugation at 10,000 r/min, washing with ultrapure water and drying at 100 °C for 12 h. As a control, the concentration effect of hydrogen peroxide solution addition was explored. The products were named Cu-S2, Cu-S5, Cu-S10, Cu-S20 when the concentration of hydrogen peroxide solution was 2 %, 5 %, 10 %, and 20 %, respectively.

2.2. Catalysts characterization

The crystal phase and textural structure of the synthesized CuO-based catalysts were characterized using X-ray powder diffraction (XRD), scanning electron microscope (SEM), transmission electron microscope (TEM), electron paramagnetic resonance (EPR), N_2 adsorption technique and synchrotron radiation X-ray absorption near-edge spectroscopy (XANES) and extended X-ray absorption fine structure (EXAFS) techniques. X-ray photoelectron spectroscopy (XPS), Fourier transform infrared spectroscopy (FTIR) and temperature programmed reduction (TPR) were used to study the surface chemical composition and redox behavior of the obtained catalysts. More details about the device configuration and test conditions see Experimental Section in [Supporting information](#).

2.3. Catalytic activity measurements

All the reduction reactions in this work were performed under mild conditions (1 atm and 25 °C) [37]. In a typical experiment, 2 mg of catalyst was added to the mixture containing NaBH₄ (0.3026 g) and 4-NP (0.16 mM, 500 mL) under mechanically stirring at 400 r/min. During hydrogenation process, 3 mL of the reaction solution was taken at intervals and analyzed on a UV-Vis spectrophotometer. The conversion of 4-NP was calculated using the value of A_t/A_0 , and the reduction kinetics of different catalysts was calculated using the equation:

$$\ln(A_t/A_0) = -kt$$

where A_t and A_0 is the absorbance (at 400 nm) of reaction solution at initial and interval time [38,39]. More details about the reaction conditions of control experiment and reusability test see Experimental Section in [Supporting information](#).

2.4. Theory calculations

The molecular-level effect of oxygen vacancy (O_v) on the atomic configuration and electronic structure of the CuO surface was studied by density functional theory (DFT) based simulations. The VASP program with the projector augmented wave (PAW) method and a plane-wave cutoff energy of 450 eV was used during theory calculations [40,41]. More calculation details see Experimental Section in [Supporting information](#).

3. Results and discussion

3.1. Morphological and structural characterizations

[Fig. 1a](#) shows the schematic diagram of the synthesis process used to prepare CuO-S30 catalysts. CuO-S_x catalysts with different oxygen vacancy (O_v) contents were prepared by a hydrothermal oxidative etching strategy using $\text{Cu}_2(\text{OH})_3\text{NO}_3$ as a precursor. Impressively, after H_2O_2 oxidative etching treatment under ambient conditions, high yields of CuO-S30 catalysts were obtained. For comparison, CuO was also

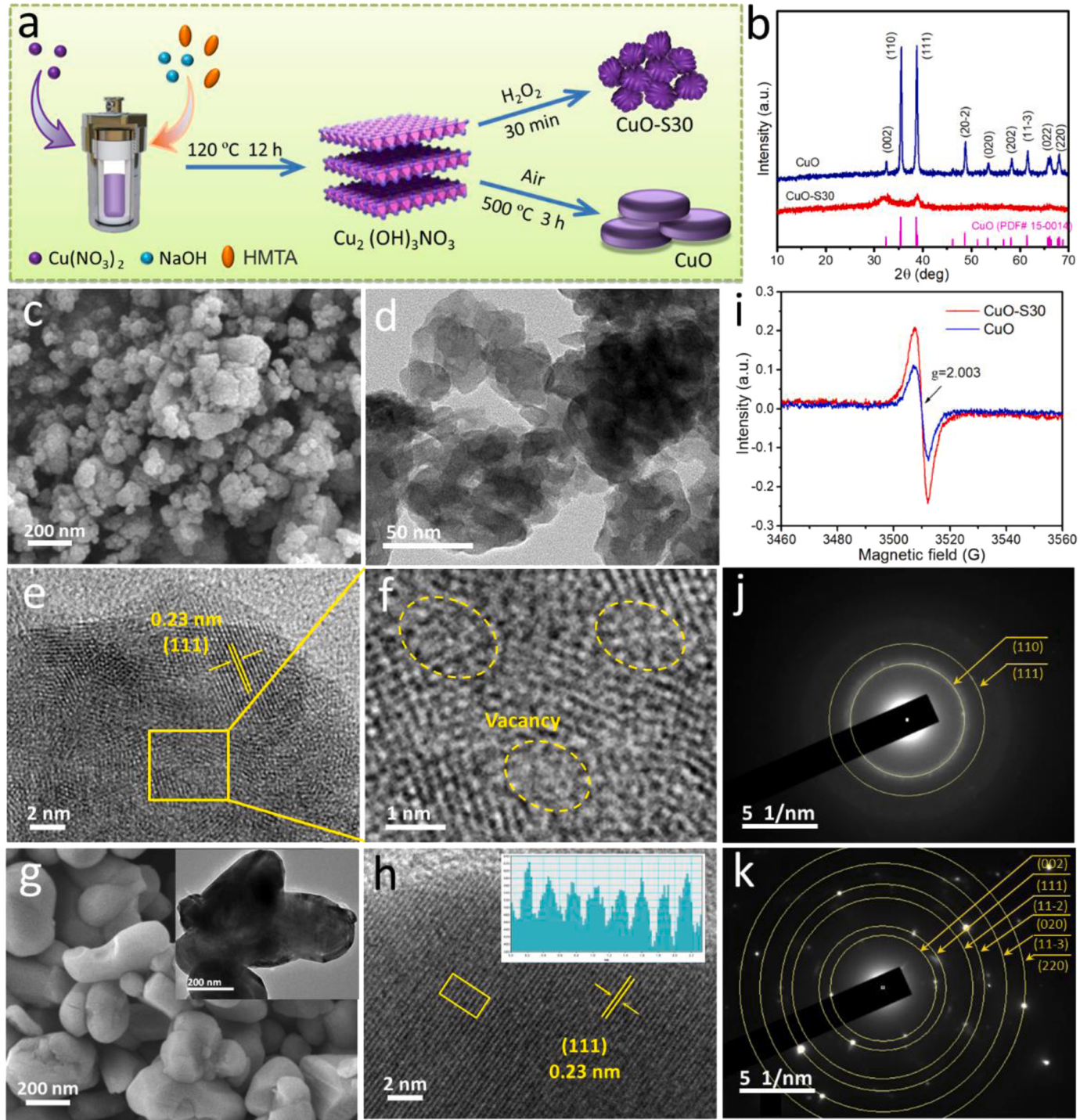


Fig. 1. (a) Schematic diagram of the preparation synthesis procedure for CuO-S30 and CuO catalyst. (b) XRD pattern of CuO-S30 and CuO catalyst. (c-f) SEM, TEM and HRTEM images of CuO-S30. (g and h) SEM, TEM and HRTEM images of CuO catalyst. (i) EPR spectra of CuO-S30 and CuO. SAED image of CuO-S30 (j) and CuO (k).

synthesized using the same Cu₂(OH)₃NO₃ precursor by conventional thermal treatment in a gas stream at 500 °C. The powder X-ray diffraction (XRD) technique was first chosen to investigate the phase structure and composition of the synthesized samples. As illustrated in Fig. 1b, sharp peaks at 32.5° (110), 35.5° (11-1), 38.7° (111), 48.7° (11-2), 53.5° (020), 58.3° (202), 61.5° (11-3), 66.2° (31-1) and 68.1° (220) appeared in the XRD pattern of CuO, confirming its high crystallinity and pure phase structure of copper oxide (JCPDS: 48-1548) [42,43]. Unlike CuO, only two broad peaks at 32.5° and 38.7° could be found in

the XRD pattern of CuO-S30, which could be indexed to (110) and (111) crystal planes, respectively. In addition, the crystalline size determined through Scherrer's formula is 11.8 nm for CuO-S30, which is obvious lower than CuO (the crystalline size is 27.9 nm), indicating a lower degree of crystallinity for CuO-S30 (Table S1). Compared with the traditional thermal treatment, the crystal transformation pathways of copper species by hydrogen peroxide treatment are different. As shown in Fig. S1, after introducing H₂O₂, the characteristic peak of Cu₂(OH)₃NO₃ precursor gradually disappeared, accompanied by the

appearance of preferentially exposed diffraction peaks of (110) and (111) in CuO-Sx samples. It is noteworthy that the intensity of the characteristic peak of CuO-Sx gradually decreased with a higher concentration of H₂O₂, confirming that the content of O_v could be justified by the concentration of hydrogen peroxide solution.

The morphologies and microstructures of CuO-S30 and normal CuO were measured by scanning electron microscopy (SEM) and transmission electron microscopy (TEM), and the results are shown in Fig. 1. The SEM image of CuO-S30 showed a uniform spherical morphology in the range of 50–200 nm (Fig. 1c and S2). The elemental mapping in Fig. S3 confirms a homogeneous distribution of the Cu and O elements. The low magnification TEM image reflects the nanoparticle-stacked structure of CuO-S30, and abundant pores could be clearly identified (Fig. 1d). This is beneficial for contributing high surface area and pore volume, thus achieving enhanced adsorption and diffusion of substrates during the catalysis process. The high-resolution TEM (HRTEM) image in Fig. 1e reveals that CuO-S30 is composed of multi-directional crystallization, which is associated with its rough surface. The identified lattice fringe space of 0.23 nm could be assigned to the (111) plane of CuO [44]. In addition, abundant vacancies, and obvious subtle lattice distortions (yellow dotted line area) were clearly detected in the HRTEM image of CuO-S30 (Fig. 1f), which is consistent with the XRD results, and is beneficial for revealing more active sites. Fig. 1g shows the SEM and TEM images of CuO synthesized by a traditional calcination route. It clearly shows an irregular granular morphology with a smooth surface and a larger particle in the range of about 200–500 nm. The HRTEM image of the CuO in Fig. 1h further confirms the high degree of crystallization, with well-defined crystalline lattices throughout the entire area of detection. The lattice fringe spacing of 0.23 nm also corresponds to the (111) plane of copper oxide. This indicates that this crystal plane is preferentially exposed for both CuO and CuO-S30.

The electron paramagnetic resonance (EPR) spectra of CuO-S30 and CuO are further measured to explore the formation of oxygen vacancy on different catalysts. As shown in Fig. 1i, identifiable signal centered at $g = 2.003$ originating from the O_v trapped electrons was detected for both CuO-S30 and CuO [45,46]. The stronger signal in the EPR spectra of CuO-S30 in comparison to CuO implies that the oxidation etching treatment with H₂O₂ leads to an increased amount of O_v on the surface of this catalyst, which agrees well with the HRTEM results. The selected area electron diffraction (SAED) image of CuO-S30 further confirmed its relatively low crystallinity (Fig. 1j). In this image, a small number of bright yellow circles with d-spacing of 0.27 nm and 0.23 nm, respectively, could be identified, which were assigned to the (110) and (111) planes. The high crystallinity of CuO is further confirmed by the bright yellow circles in the SAED image. The diffraction spots with d-spacing of 0.253 nm, 0.232 nm, 0.196 nm, 0.171 nm, 0.151 nm, and 0.138 nm corresponded well to the (002), (111), (11–2), (020), (11–3), and (220) crystal planes of the CuO phase, respectively (Fig. 1k) [47,48]. Such abundant O_v active sites of the catalysts can modulate the electronic properties of the materials, thus achieving improved performance during the catalytic process.

The surface area and pore structure of the obtained oxides were characterized by means of N₂ adsorption technology, and the textural parameters are shown in Fig. S4 and Table S1. As shown, CuO-S30 exhibits typical IV isotherms with an obvious hysteresis loop at relative pressure of 0.45–1.0. In the meantime, a sharp peak appears at ca. 3.7 nm in the pore size distribution curve of CuO-S30, which reflects the mesoporous structure of this sample [49,50]. As for CuO, IV isotherms with hysteresis loop are also detected in the relative pressure range of 0.75–1.0. As summarized in Table S1, the calculated surface area (S_{BET}) and pore volume for CuO-S30 are 179 m²/g and 0.32 cm³/g, respectively. However, CuO showed a relatively lower surface area and pore volume of 110 m²/g and 0.19 cm³/g, respectively, due to the collapse of the hydroxide precursor after the calcination at high temperatures.

The detailed coordination environments of specific Cu atoms in CuO-S30 and CuO were investigated by synchrotron radiation X-ray

absorption near-edge spectroscopy (XANES) and extended X-ray absorption fine structure (EXAFS) techniques. The standard samples of copper foil and Cu₂O were used as reference materials. As shown in Fig. 2a, the Cu K-edge XANES spectrum of CuO-S30, including the energy absorption edge and the white line peak, is similar to that of CuO, with a clear difference from that of copper foil and Cu₂O, which confirms that Cu²⁺ is the dominant copper species in both samples [51]. Compared to CuO, the slight red shift in the absorption edge of CuO-S30 indicates a positively charged electron structure in the Cu²⁺ species. In addition, a characteristic pre-edge peak at about 8985.8 eV was identified for both CuO-S30 and CuO (Fig. 2a, inset). This peak was attributed to tetragonal coordinated Cu centers due to the Jahn-Teller effect [52]. Additionally, the decrease in intensity of the pre-edge peak for CuO-S30 further reveals the unsaturated Cu-O coordination and O_v-rich structure.

Fig. 2b shows the Fourier transform of the Cu K-edge EXAFS of CuO-S30, CuO and copper foil, and Cu₂O reference. Only one peak assigned to the metallic Cu-Cu coordination at 2.23 Å is observed for the Cu foil. In addition to the Cu-Cu coordination at 2.70 Å, Cu-O coordination at 1.47 Å was obtained in the EXAFS spectra of Cu₂O. As for CuO-S30 and CuO, similar coordination modes of Cu-Cu and Cu-O were detected at 1.54 Å and in the range of 2.50–3.24 Å, respectively. The similar coordination environment of Cu atoms in CuO-S30 and CuO compared to that of Cu foil and Cu₂O is further confirmed by the wavelet transform (WT) of the Cu K-edge EXAFS spectra in Fig. 2c. In addition, by fitting the Cu K-edge EXAFS spectrum using Artemis software, the structural configurations for CuO-S30 and CuO were further extracted (Table S2). The optimal fitting curves in R-space and k-space are shown in Fig. 2d and e, respectively. For the CuO catalyst, the first shell consists of four O atoms and the second shell consists of three Cu-Cu pathways with a coordination number (CN) of 9.6. However, the CNs of both the first shell (3.1) and the second shell (3.4) are decreased for CuO-S30 (Table S2 and Fig. 2d). This undoubtedly confirms the abundant O_v in this catalyst, which is beneficial for the adsorption and activation of substrates on active sites during catalytic transformation.

The valence states of the Cu sites on the CuO-based catalysts were further investigated by X-ray photoelectron spectroscopy (XPS). High-resolution Cu 2p and O 1s XPS spectra of CuO-S30 and CuO are shown in Fig. 3, respectively. In the binding energy region of Cu (Fig. 3a), the two main peaks at 934.5 eV and 954.5 eV are attributed to Cu2p^{3/2} and Cu2p^{1/2}, respectively [53]. Meanwhile, the strong satellite peaks at 943 eV further confirmed that the predominant valence of the copper species is +2, which is in good agreement with the XRD results. In addition, the center of the Cu 2p peaks for CuO-S30 left shifts to higher binding energies with 0.39 eV compared to that for CuO, suggesting a positively charged nature of the Cu sites in CuO-S30, which could be attributed to the charge reconstruction effect induced by the oxygen vacancies. This is also confirmed by the different energy distribution in the XPS spectra of O 1s for CuO-S30 and CuO (Fig. 3b). According to the literature [54,55], the O 1s peaks are deconvoluted into three peaks at 528.8, 529.7 and 533.1 eV, which can be attributed to lattice oxygen (O_L, peak I), oxygen vacancies or interfacial oxygen species (O_v, peak II) and OH groups from adsorbed H₂O (O_W, peak III), respectively. The amount of O_v could be qualitatively determined based on the area of the corresponding peaks. The ratio between the area of peak II and peak I is found to be about 3 for CuO-S30, while it dramatically decreases to 0.5 for CuO, indicating the more abundant O_v species in the CuO-S30.

The Fourier transform infrared (FT-IR) spectra of CuO-S30 and CuO are shown in Fig. 3c. The similar stretching mode of the Cu-O bonds around 559 cm⁻¹ indicates a similar valence-bond structure for both solids [42]. However, CuO-S30 shows a much stronger -OH antisymmetric stretching vibration at 3445 cm⁻¹ than that of CuO. As shown in the inset of Fig. 3c, both of materials could be readily dispersed into water to form the corresponding suspensions, and the Tyndall effect could be clearly observed in the suspensions with a brighter light path

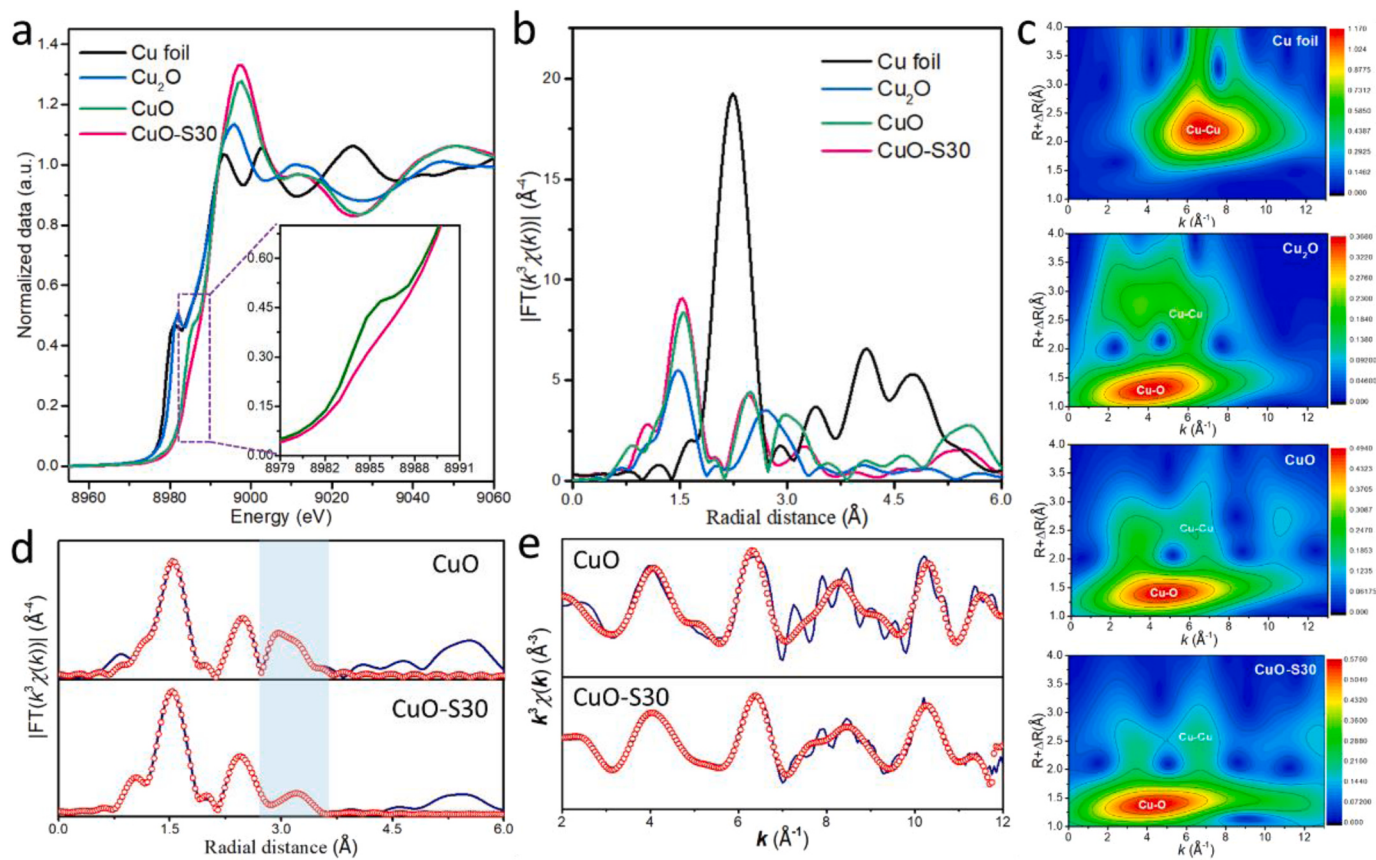


Fig. 2. (a) Cu X-ray absorption near structure (XANES) spectra and (b) Fourier transform of the Cu K-edge EXAFS of CuO-S30, CuO and reference samples Cu foil, Cu₂O (Inset: enlargement of the selected area). (c) Wavelet transforms for the EXAFS signals for the Cu-based catalysts. EXAFS fitting curve in R space (d) and k space (e) of CuO-S30 and CuO catalysts.

for CuO-S30. Such a facile dispersion characteristic in the water for the materials is advantageous to increase the probability of collision between the catalyst and the reactants, thus improving the catalytic performance. In addition, the redox properties of CuO-S30 and CuO were also characterized by the temperature programmed reduction (TPR) technique, and the results are shown in Fig. 3d. For CuO, the TPR curve shows an initial reduction temperature of 203 °C, followed by two reduction peaks at 329 °C and 413 °C, resulting from the reduction of Cu²⁺ to Cu⁰ [42,56]. For the oxygen vacancy functionalized CuO-S30 catalyst, a significantly lower initial reduction temperature of 128 °C was observed in the TPR profile, accompanied by the appearance of three reduction peaks at 243 °C, 292 °C and 401 °C, respectively. These newly appeared peaks at the lower temperature ranges undoubtedly confirm the higher reducibility of CuO-S30, which should be an advantage for its usage in catalyzing reactions with a redox process.

3.2. Catalytic performance of 4-NP reduction

To evaluate the catalytic behavior of the obtained materials, the catalytic reduction of 4-NP was selected as a model reaction using NaBH₄ as the hydrogen source. Fig. 4 summarizes the catalytic performance of the CuO-based catalyst in the model reaction. All the reactions were carried out at room temperature and under atmospheric conditions (25 °C and 1 atm.). As shown in Fig. S5, the UV-Vis absorption of the 4-NP solution was significantly red-shifted from 317 nm to 400 nm after the addition of NaBH₄, confirming the formation of phenolic ions under alkaline conditions [39,57]. No decrease in the intensity of the maximum absorption wavelength was detected in the absence of any catalyst (Fig. S6), which indicates that the hydrogenation reaction has a high activation energy, and NaBH₄ cannot reduce the reactant

spontaneously without any catalyst. After the addition of CuO-S30, as shown in Fig. 4a, the intensity of the characteristic peak for 4-NP decreased rapidly with the fading of the light-yellow solution to colorless (Fig. S7), confirming its superior capability for 4-NP conversion. From Fig. 4b, both CuO-S30 and CuO are active in catalyzing the reduction of 4-NP. However, 84 % conversion of 4-NP was obtained after 30 min of reaction over CuO. For CuO-S30, the complete conversion of 4-NP takes only 5 min. Thus, a significantly higher performance is achieved. Notably, the concentration of hydrogen peroxide not only affects the microstructure of the obtained catalyst, but also influences its activity in reducing 4-NP. As shown in Fig. 4c, by increasing the hydrogen peroxide concentration, a superior activity of the obtained catalyst was achieved. The 4-NP conversion after 5 min of reaction is in accordance with the trends: CuO-S30 > CuO-S20 > CuO-S10 > CuO-S5 > CuO-S2 > CuO, indicating that the hydrogen peroxide oxidation etching method is beneficial for further improving the catalytic activity of the CuO catalyst.

Encouraged by the excellent performance of CuO-S30 in reducing 4-NP, the effect of reaction conditions on the catalytic behavior was investigated in detail. As shown in Fig. 4d, an obvious improvement in the catalytic performance was achieved by increasing the catalyst dosage from 0.5 mg to 4 mg, and the complete conversion of 4-NP decreased to only 3 min at a catalyst dosage of 4 mg. The reaction time for the 80 % conversion of 4-NP is 46 s, 117 s, 175 s, and 286 s for the catalyst dosage of 4 mg, 2 mg, 1 mg, and 0.5 mg, respectively (Fig. 4d, inset). It is noteworthy that even with a catalyst dosage of 0.5 mg, the conversion of 4-NP was higher than 92.3 % after a prolonged reaction. This confirms the excellent capability of CuO-S30 for 4-NP reduction. Fig. 4e shows the effect of the molar ratio of the reactants on the catalytic activity of CuO-S30. A large improvement in catalytic

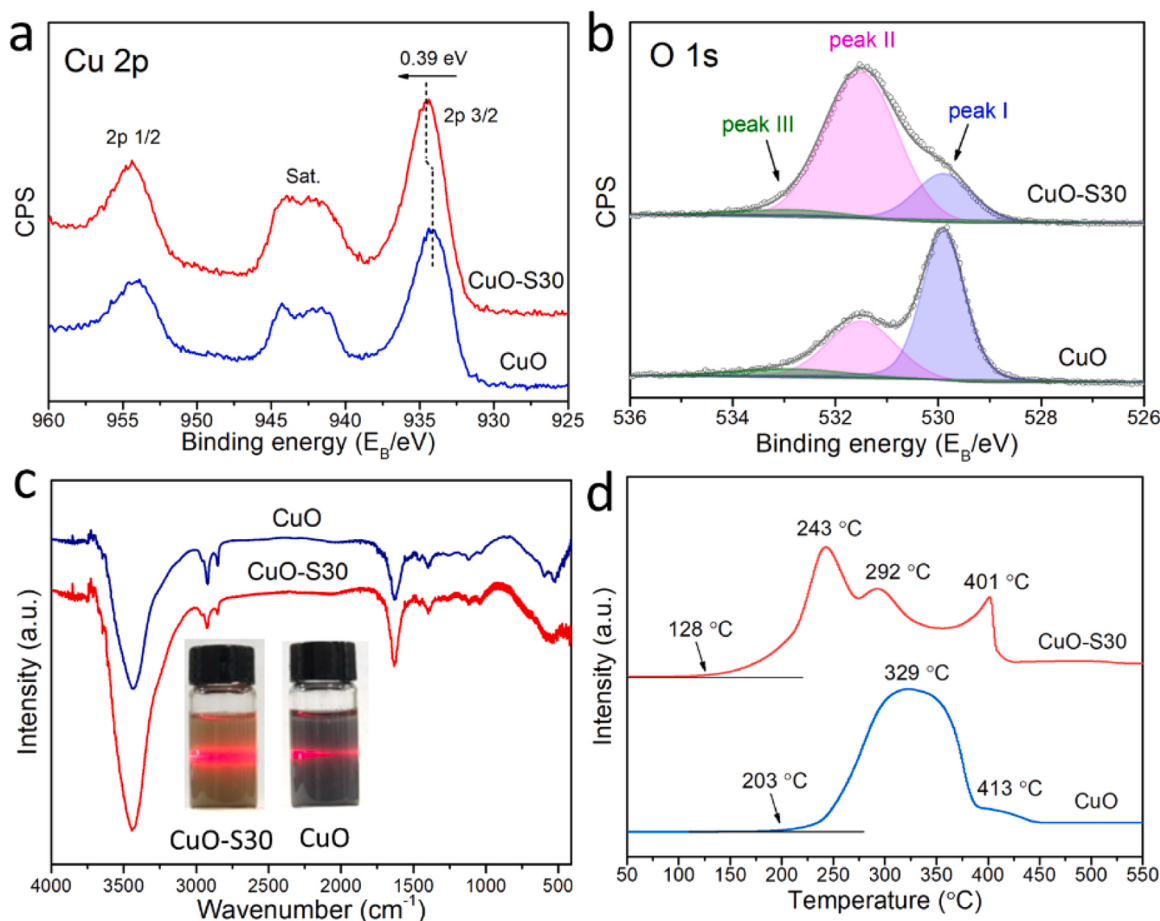


Fig. 3. (a) High-resolution XPS signals of Cu 2p and (b) O 1 s in CuO-S30 and CuO. (c) FT-IR signals of CuO-S30 and CuO (the inset shows the Tyndall effect of the catalyst suspension). (d) H₂-TPR signals of CuO-S30 and CuO.

activity was observed by increasing the molar ratio of NaBH₄:4-NP from 50:1 to 100:1. This was due to the occurrence of more effective collisions between the substrate molecules. However, when the molar ratio was further increased from 100:1 to 200:1, a similar performance was observed. Furthermore, the catalytic performance of 4-NP reduction under different reaction temperatures (5, 15, 25, and 35 °C) is shown in Fig. 4f. It can be clearly seen that an improved catalytic performance was obtained for CuO-S30 under a higher reaction temperature. For example, the reaction time for the complete reduction of 4-NP decreased from 30 min to 4 min with the temperature increase from 5 °C to 35 °C. This indicates that the title reaction is a thermodynamically favorable process over CuO-S30.

In addition to the reduction of 4-NP, as shown in Fig. 4g and Table S3, CuO-S30 also exhibited robust capability for the catalytic reduction of nitrobenzene compounds with different molecular conformations and with different functional groups of -C=O, -CH₃, -Cl and so on. For example, the reaction time for the complete conversion of 2-NP and 3-NP is 4 min and 3 min, respectively. The reusability of the catalyst is one of the most important properties of the catalyst, especially in practical applications. Therefore, the stability and reusability of CuO-S30 were evaluated by cyclic catalysis experiments, and the results are shown in Fig. 4h. After 5 cycles of catalysis, the conversion of 4-NP catalyzed by CuO-S30 was still above 90 %, indicating its excellent catalytic stability. In addition, the morphology and O_v could be well preserved based on the analysis from the SEM images (Fig. S8) and XPS spectra (Fig. S9) of the reused CuO-S30. The unique high stability and recyclability are intriguing properties for CuO-S30 catalyst, as the morphological and surficial transformation in metal oxides have been closely related to the activity degradation of these catalysts, even

leading to inactivation in certain cases.

3.3. Kinetics and thermodynamics of 4-NP reduction

The reaction kinetics of the catalytic reduction of 4-NP over CuO catalysts has also been studied. The reduction rate can be correlated with the amount of 4-NP because excess NaBH₄ was used during the reaction process. Fig. 4i shows the kinetic curves of 4-NP reduction over the CuO-S30 and CuO catalysts. A linear relationship between ln(A_t/A₀) and reduction time (t) was obtained, which is similar to the results from X. Zhao et al. [22]. Therefore, a pseudo-first-order kinetic model was used to calculate the kinetic rate of the reaction using the equation: ln(A_t/A₀) = -kt, where k is the rate constant of the reaction. Through the fitting of the reaction rate data, the calculated value of the rate constant (k) is $1.13 \times 10^{-3} \text{ s}^{-1}$ for CuO. In contrast, the value of k for CuO-S30 was calculated to be up to $15.7 \times 10^{-3} \text{ s}^{-1}$. This means that CuO-S30 has a reduction kinetic 13 times that of the CuO catalyst. In addition, the k of 4-NP catalyzed by CuO-S30 was significantly higher than that of most Cu-containing catalysts reported in the literature, and even close to or better than that of some precious metal-based catalysts (Fig. 4j, Table S4).

By evaluating the catalytic kinetics of the 4-NP reduction under different reaction temperatures, the reaction thermodynamics for the CuO-S30 and CuO catalysts were also investigated. The kinetic curves and linearly fitted results in Fig. S10 show an increase in the rate constant (k) at higher reaction temperatures, indicating that the reaction is thermodynamically favorable for both catalysts. Using the calculated k of 4-NP reduction at different temperatures (T), the plots of lnk vs. 1/T are shown in Fig. 4k. It is obvious that a good linear fit was obtained for

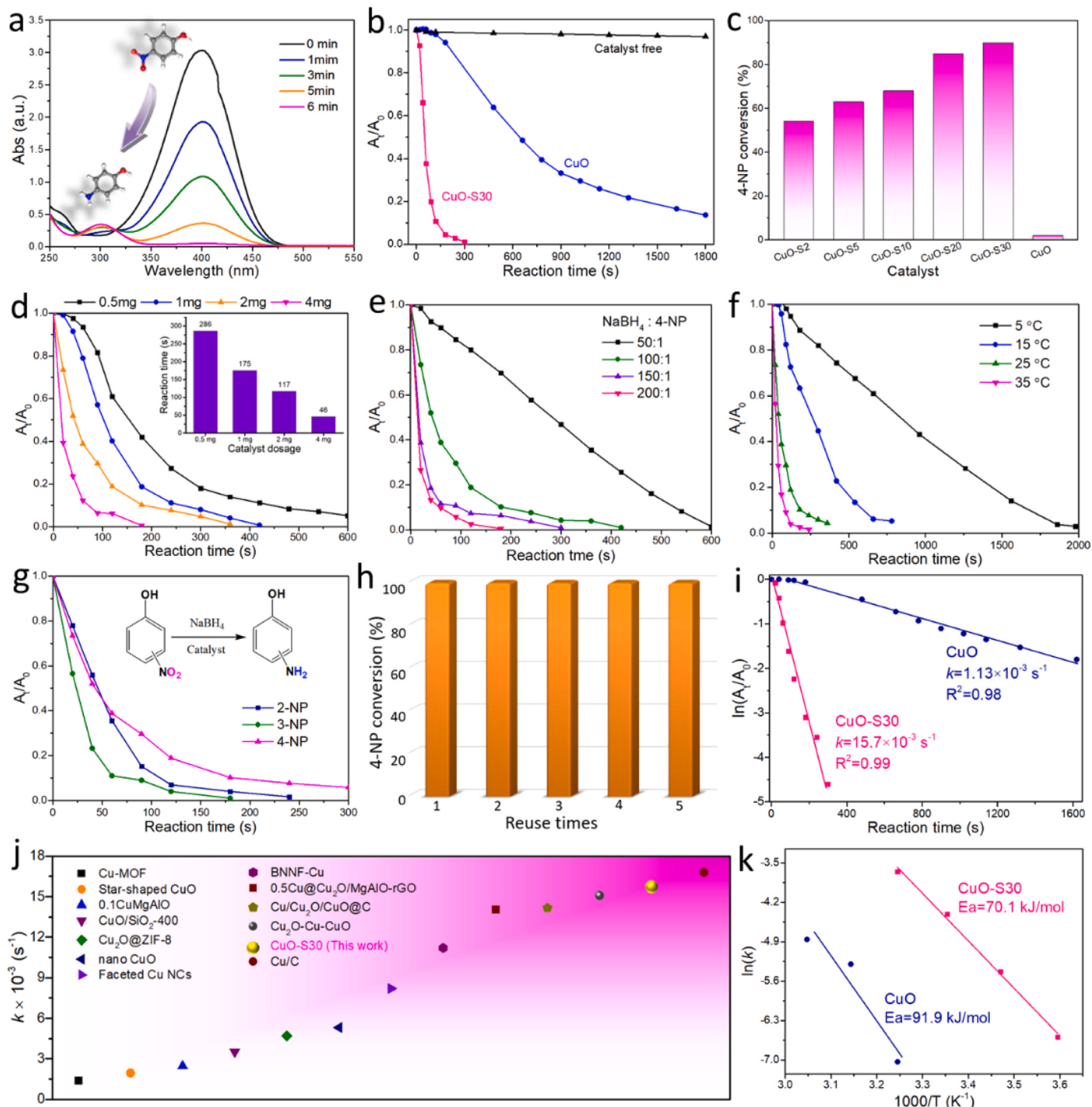


Fig. 4. (a) The evolution of UV-vis spectra of the 4-NP solution with the addition of CuO-S30. (b) Catalytic performance of CuO-S30 and CuO in 4-nitrophenol hydrogenation. (c) 4-NP conversion over different CuO-Sx catalysts after 5 min reaction. (d) The effect of catalyst dosage on the catalytic activity of 4-NP reduction over CuO-S30 (the inset showed the reaction time for 80 % of 4-NP conversion). The effect of the (e) ratio of reactants and (f) reaction temperature on the catalytic performance of CuO-S30 for 4-NP reduction. (g) The catalytic performance of CuO-S30 for the reduction of different nitrophenols. (h) The performance of CuO-S30 for the repeated catalytic reduction of 4-NP. (i) The kinetics and rate constants of 4-NP reduction catalyzed by CuO-S30 and CuO. (j) Performance comparison of different Cu-based catalysts for 4-NP reduction. (k) The activation energy of CuO-S30 and CuO in catalyzing the reduction of 4-NP.

both the CuO-S30 and the CuO catalysts. Additionally, activation energy (Ea) was calculated from the linear fit slope (Ea/R) based on the classical Arrhenius equation. For CuO and CuO-S30 catalysts, the values of Ea are 91.9 kJ/mol and 70.1 kJ/mol, respectively. The lower activation energy over CuO-S30 means lower energy consumption during 4-NP activation, which should be responsible for its superior catalytic performance.

3.4. Catalytic mechanisms

From previous works, the efficient adsorption of the reactant molecule and especially the subsequent catalyst-mediated electron transfer from hydrogen donor to 4-NP are the main rate-determining steps for 4-NP reduction. Based on the results of XRD, HRTEM, EPR, XAFS, and XPS, CuO structure with oxygen vacancy (denoted as CuO-O_V) and crystalline CuO were further constructed as models by DFT to investigate the effects

of O_v on the microstructure, electronic property, and substrate activation behavior during the 4-NP reduction process. Fig. 5a-f show the optimized atomic configurations in side-view and top-view on (111) facets of CuO-O_v and CuO , as the corresponding plane was dominated for both samples according to the TEM image and XRD results. The Cu and O atoms in CuO show a symmetrical spatial configuration with a distance of 2.88 Å for Cu1-Cu2 and 3.00 Å Cu2-Cu3, respectively. For CuO-O_v , as shown in Fig. 5d and e, an extended distance of 3.79 Å and the shortened distance of 2.92 Å were obtained for Cu1-Cu2 and Cu2-Cu3, respectively. These results showed that the atomic configuration gets rearranged with the formation of O_v , especially for the atoms

adjacent to O_v . The influence of the change in the catalyst microstructure on the electronic properties is further demonstrated by the electronic change of the d-orbital of the Cu atom (Table S5). Compared to CuO , the charge density difference becomes delocalized for CuO-O_v , which should be caused by the redistribution of charge density during O_v formation (Figs. 5c, f and Fig. S11). Fig. S12 shows that CuO-O_v has a higher adsorption energy of 4-NP ($E_{\text{ads}} = -1.530$ eV) compared with CuO ($E_{\text{ads}} = -1.109$ eV), indicating that CuO-O_v is more favorable for 4-NP adsorption. Meanwhile, the desorption energy (E_{des}) of 4-AP on CuO-O_v is 0.762 eV, this value is lower than that of CuO ($E_{\text{des}} = 0.972$), which could benefit the recovery of active sites during catalytic process.

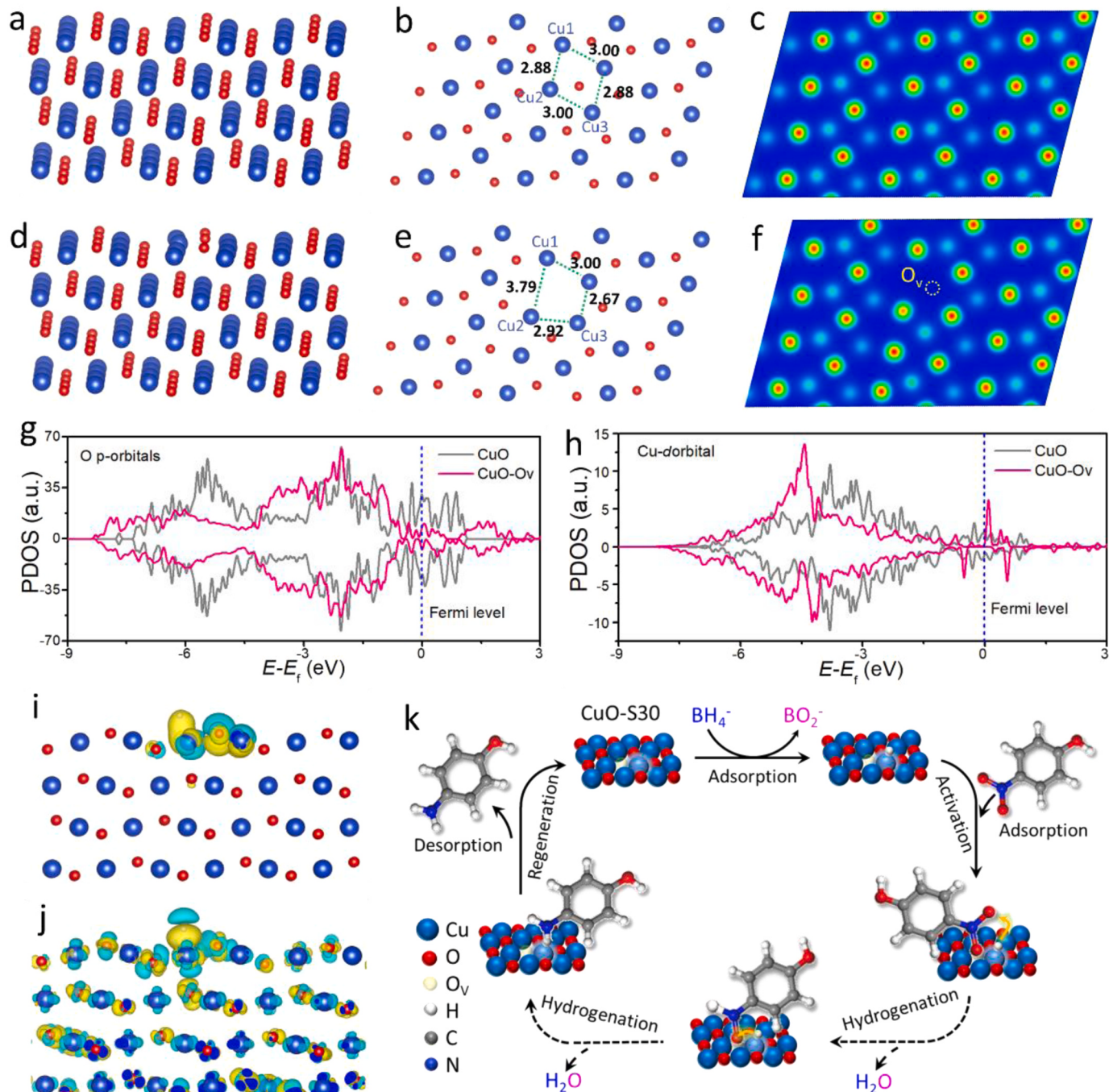


Fig. 5. The side view, top view, and electronic localization function (ELF) contour of CuO (a-c) and CuO-O_v (d-f). Partial density of states (PDOS) of Cu and O on CuO and CuO-O_v (g and h). The differential charge distribution of H adsorbed on CuO (i) and CuO-O_v (j) during hydrogen activation. (k) Schematic mechanism illustration of the 4-NP reduction on CuO-S30 .

The detailed partial density of states (PDOS) spectra of O and Cu for both samples are shown in Fig. 5g and h. Due to the loss of oxygen atoms, CuO-O_v showed a decreased O-PDOS around the Fermi level. On the other hand, the Cu PDOS in CuO-O_v increased near the Fermi level compared to CuO. This would promote electron transformation during the reactant activation and product desorption process. Tong *et al.* have previously demonstrated that the ability to activate hydrogen species and transform electrons is crucial for the catalysts during the reduction of 4-NP [58]. Fig. 5i and j shows the charge density difference of H adsorption on CuO and CuO-O_v. It can be clearly seen that the hydrogen atoms are preferentially adsorbed at the Cu site on the surface of both samples, which indicates that the Cu atoms on the surface are the main active sites for the activation of H. In addition, for CuO, the electron depletion area is mainly concentrated in the surface layer. Except for the surface layer, the electron depletion area appears in the bottom atoms of CuO-O_v. These results confirm its stronger charge transfer capability, which should be responsible for its lower activation energy and superior performance for 4-NP reduction.

Through a combined analysis of experimental and theoretical results, the significant role of oxygen vacancies in CuO-S30 for the highly efficient reduction of 4-NP under mild conditions could be ascribed to the following reasons: (i) introducing O_v provides abundant unsaturated surface Cu sites with positively charged properties, which are helpful for adsorbing negatively charged substrate molecules via electrostatic interaction; (ii) the generation of O_v also triggers the rearrangement and electron delocalization of metal sites on the surface of the catalyst, which could facilitate the activation of the adsorbed substrates and achieve rapid electron transfer during the conversion, which synergistically leads to the efficient conversion. A hypothetical mechanism for the 4-NP reduction catalyzed by O_v-containing CuO-S30 is shown in Fig. 5k. Initially, the negatively charged molecules of BH₄ and 4-NP⁻ were easily adsorbed on the positively charged Cu sites due to the strong substrate-active site interaction. Benefiting from the stronger electron-injecting capacity of H-donor and the highly activated H species subsequently attract the O₂N groups of nearby 4-NP and reduce them to 4-AP through a continuous hydrodeoxygenation process. The final desorption of 4-AP completes the reduction cycle, releasing active Cu sites for the next cycle.

4. Conclusion

In summary, structural reconfiguration and O_v construction were achieved at ultrafast rates and under green conditions for the CuO-S30 catalyst obtained by a combined ultrasonic and H₂O₂ oxidation etching. Compared with bulk CuO, CuO-S30 achieved 13 times higher kinetics, significantly reduced activation energy, and exceptional reusability for the reduction of 4-NP under mild conditions. The combined structural characterizations and DFT simulations confirmed the key role of O_v in modulating the structural/electronic configurations of CuO-S30, which promotes reactant trapping through electrostatic interaction and enhances electron transfer during 4-NP reduction process. This work contributes a facile route for electronic structure regulation of metal oxides through O_v creating, and a case study about structure-activity relationship that could provide important implications for designing advanced catalyst with high catalytic performance.

CRediT authorship contribution statement

Longlong Geng: Methodology, Conceptualization, Writing – review & editing. **Qing Zhang:** Investigation. **Xiaoli Wang:** Software, Writing – review & editing. **Hanhai Xiang:** Formal analysis. **Yong-Zheng Zhang:** Writing – review & editing. **Chunhui Li:** Investigation. **Zhen Li:** Formal analysis. **Da-Shuai Zhang:** Methodology, Formal analysis. **Xiuling Zhang:** Methodology, Project administration. **Abdukader Abdulkayum:** Formal analysis, Resources. **Guangzhi Hu:** Conceptualization, Funding acquisition, Writing – review & editing.

Declaration of Competing Interest

The authors declare that they have no known competing financial interests or personal relationships that could have appeared to influence the work reported in this paper.

Data Availability

Data will be made available on request.

Acknowledgments

This work was financially supported by the National Natural Science Foundation of China (21902022, 22103010), Qingchuang Science and Technology Plan of Shandong Province (2021KJ054), the Natural Science Foundation of Shandong Province (ZR2018LB018, ZR2019QB026, ZR2020KB014, ZR2022QB058), Double-First Class University Plan (C176220100042), Tianshan Innovation Team Plan of Xinjiang Uygur Autonomous Region (2023D14002), Science and Technology Plan of Dezhou (2022dzkj004), Scientific Research Foundation of Dezhou University (2023XKZX005, 2023xjrc210, 2021xjrc309). The authors also thank the support of XAS tests from HUASUANTECHNOLOGY.

Appendix A. Supporting information

Supplementary data associated with this article can be found in the online version at doi:10.1016/j.apcatb.2023.123575.

References

- [1] A. Li, H. Pang, P. Li, N. Zhang, G. Chen, X. Meng, M. Liu, X. Liu, R. Ma, J. Ye, Insights into the critical dual-effect of acid treatment on ZnxCd_{1-x}S for enhanced photocatalytic production of syngas under visible light, *Appl. Catal. B: Environ.* 288 (2021), 119976.
- [2] W. Wang, Y. Liu, Y. Yue, H. Wang, G. Cheng, C. Gao, C. Chen, Y. Ai, Z. Chen, X. Wang, The confined interlayer growth of ultrathin two-dimensional Fe₃O₄ nanosheets with enriched oxygen vacancies for peroxyomonosulfate activation, *ACS Catal.* 11 (2021) 11256–11265.
- [3] W. Zhu, X.-b Wang, C. Li, X. Chen, W.-y Li, Z. Liu, C. Liang, Defect engineering over Co₃O₄ catalyst for surface lattice oxygen activation and boosted propane total oxidation, *J. Catal.* 413 (2022) 150–162.
- [4] F. Li, A. Thevenon, A. Rosas-Hernández, Z. Wang, Y. Li, C.M. Gabardo, A. Ozden, C. T. Dinh, J. Li, Y. Wang, J.P. Edwards, Y. Xu, C. McCallum, L. Tao, Z.-Q. Liang, M. Luo, X. Wang, H. Li, C.P. O'Brien, C.-S. Tan, D.-H. Nam, R. Quintero-Bermudez, T.-T. Zhuang, Y.C. Li, Z. Han, R.D. Britt, D. Sinton, T. Agapie, J.C. Peters, E. H. Sargent, Molecular tuning of CO₂-to-ethylene conversion, *Nature* 577 (2020) 509–513.
- [5] H. Gao, S. Ning, J. Lin, X. Kang, Molecular perturbation of 2D organic modifiers on porous carbon interlayer: promoted redox kinetics of polysulfides in lithium-sulfur batteries, *Energy Storage Mater.* 40 (2021) 312–319.
- [6] M. Sun, Y. Wang, C. Sun, Y. Qi, J. Cheng, Y. Song, L. Zhang, Nitrogen-doped Co₃O₄ nanowires enable high-efficiency electrochemical oxidation of 5-hydroxymethylfurfural, *Chin. Chem. Lett.* 33 (2022) 385–389.
- [7] Q. Luo, C. Lu, L. Liu, M. Zhu, A review on the synthesis of transition metal nitride nanostructures and their energy related applications, *Green. Energy Environ.* 8 (2023) 406–437.
- [8] X. Jia, X. Zhao, Z. Bi, H. Zhang, S. Huang, J. Chun-Ho Lam, W. Li, Y. Li, T. Wågberg, G. Hu, Rod-shaped lanthanum oxychloride-decorated porous carbon material for efficient and ultra-fast removal of phosphorus from eutrophic water, *Sep. Purif. Technol.* 306 (2023), 122713.
- [9] Z.-X. Wei, Y.-T. Zhu, J.-Y. Liu, Z.-C. Zhang, W.-P. Hu, H. Xu, Y.-Z. Feng, J.-M. Ma, Recent advance in single-atom catalysis, *Rare Met.* 40 (2021) 767–789.
- [10] Z. Li, W. Wei, H. Li, S. Li, L. Leng, M. Zhang, J.H. Horton, D. Wang, W. Sun, C. Guo, W. Wu, J. Wang, Low-temperature synthesis of single palladium atoms supported on defective hexagonal boron nitride nanosheet for chemoselective hydrogenation of cinnamaldehyde, *ACS Nano* 15 (2021) 10175–10184.
- [11] Z. Li, X. Lu, W. Sun, L. Leng, M. Zhang, H. Li, L. Bai, D. Yuan, J.H. Horton, Q. Xu, J. Wang, One-step synthesis of single palladium atoms in WO_{2.72} with high efficiency in chemoselective hydrodeoxygenation of vanillin, *Appl. Catal. B: Environ.* 298 (2021), 120535.
- [12] F. Zhang, J. Fang, L. Huang, W. Sun, Z. Lin, Z. Shi, X. Kang, S. Chen, Alkyne-functionalized ruthenium nanoparticles: impact of metal-ligand interfacial bonding interactions on the selective hydrogenation of styrene, *ACS Catal.* 9 (2019) 98–104.
- [13] J. Wang, F. Zhang, X. Kang, S. Chen, Organic functionalization of metal catalysts: enhanced activity towards electroreduction of carbon dioxide, *Curr. Opin. Electrochem.* 13 (2019) 40–46.

[14] Z. Li, L. Leng, X. Lu, M. Zhang, Q. Xu, J.H. Horton, J. Zhu, Single palladium atoms stabilized by β -FeOOH nanorod with superior performance for selective hydrogenation of cinnamaldehyde, *Nano Res.* 15 (2022) 3114–3121.

[15] J. Lin, Y. Zhou, J. Wen, W. Si, H. Gao, G. Wang, X. Kang, Pyrrole derivatives as interlayer modifier of Li-S batteries: modulation of electrochemical performance by molecular perturbation, *J. Energy Chem.* 75 (2022) 164–172.

[16] J. Kuczyńska, A. Pawlak, B. Nieradko-Iwanicka, The comparison of dexketoprofen and other painkilling medications (review from 2018 to 2021), *Biomed. Pharmacother.* 149 (2022), 112819.

[17] M. Sharafee Shamsudin, A. Taufik Mohd Din, L. Sellaoui, M. Badawi, A. Bonilla-Petriciolet, S. Ismail, Characterization, evaluation, and mechanism analysis of the functionalization of kaolin with a surfactant for the removal of diclofenac from aqueous solution, *Chem. Eng. J.* 465 (2023), 142833.

[18] Z. Li, C. Han, Palladium nanoflowers supported on amino-fullerene as novel catalyst for reduction of 4-nitrophenol, *Chin. Chem. Lett.* 31 (2020) 818–820.

[19] Z. Li, M. Zhang, X. Dong, S. Ji, L. Zhang, L. Leng, H. Li, J.H. Horton, Q. Xu, J. Zhu, Strong electronic interaction of indium oxide with palladium single atoms induced by quenching toward enhanced hydrogenation of nitrobenzene, *Appl. Catal. B: Environ.* 313 (2022), 121462.

[20] Y. Sheng, Y. Liu, Y. Yin, X. Zou, J. Ren, B. Wu, X. Wang, X. Lu, Rh promotional effects on Pt–Rh alloy catalysts for chemoselective hydrogenation of nitrobenzene to p-aminophenol, *Chem. Eng. J.* 452 (2023), 139448.

[21] X. Zhuang, K. Jin, Q. Zhang, J. Liu, X. Zhang, H. Zhan, L. Ma, One-pot synthesis of Fe_3O_4 nanoparticles embedded within N-doped carbon layers as highly efficient and selective catalysts for the hydrogenation of nitroarenes, *Chin. Chem. Lett.* 34 (2023), 107954.

[22] Y. Wang, Z. Bi, X. Zhao, A. Abdukayum, S. Zhou, H. Zhang, J. Chen, F. Tan, A. Chen, T. Wågberg, G. Hu, Fast room-temperature hydrogenation of nitroaromatics on Pd nanocrystal–boron cluster/graphene oxide nanosheets, *Mol. Catal.* 529 (2022), 112543.

[23] R. Dey, N. Mukherjee, S. Ahmed, B.C. Ranu, Highly selective reduction of nitroarenes by iron(0) nanoparticles in water, *Chem. Commun.* 48 (2012) 7982–7984.

[24] Y. Ma, Z. Lang, J. Du, L. Yan, Y. Wang, H. Tan, S.U. Khan, Y. Liu, Z. Kang, Y. Li, A switchable-selectivity multiple-interface Ni–WC hybrid catalyst for efficient nitroarene reduction, *J. Catal.* 377 (2019) 174–182.

[25] N. Pravin, G. Kumaravel, V. Muniyandi, P.P. Utthra, N. Raman, A study on the role of dicarboxylic acid conjugated Copper(II) complexes in the reduction of p-nitrophenol under mild condition in water medium, *Energy Environ. Focus* 6 (2017) 184–192.

[26] B. Lang, H.-K. Yu, Novel Ag2S nanoparticles on reduced graphene oxide sheets as a super-efficient catalyst for the reduction of 4-nitrophenol, *Chin. Chem. Lett.* 28 (2017) 417–421.

[27] X. Zhang, N. Wang, L. Geng, J. Fu, H. Hu, D. Zhang, B. Zhu, J. Carozza, H. Han, Facile synthesis of ultrafine cobalt oxides embedded into N-doped carbon with superior activity in hydrogenation of 4-nitrophenol, *J. Colloid Interface Sci.* 512 (2018) 844–852.

[28] Z. Zhang, M. Zhou, Y. Chen, S. Liu, H. Wang, J. Zhang, S. Ji, D. Wang, Y. Li, Pd single-atom monolithic catalyst: Functional 3D structure and unique chemical selectivity in hydrogenation reaction, *Sci. China Mater.* 64 (2021) 1919–1929.

[29] L. Zhu, Y. Sun, H. Zhu, G. Chai, Z. Yang, C. Shang, H. Ye, B.H. Chen, A. Kroner, Z. Guo, Effective ensemble of Pt single atoms and clusters over the (Ni,Co)(OH)₂ substrate catalyzes highly selective, efficient, and stable hydrogenation reactions, *ACS Catal.* 12 (2022) 8104–8115.

[30] J.-J. Fang, Q.-M. Liu, X.-W. Kang, S.-W. Chen, Selective hydrogenation of 4-nitrostyrene to 4-nitroethylbenzene catalyzed by Pd@Ru core–shell nanocubes, *Rare Met.* 41 (2022) 1189–1194.

[31] Y. Wang, X. Zhao, J. Chen, S. Zhou, X. Zhang, X. Wang, T. Wågberg, G. Hu, Dodecahydrododecaborate anion cluster-reduced nano-Au-decorated graphene oxide for 100% hydrogenation of nitroaromatics, *Colloid Interface Sci. Commun.* 50 (2022), 100672.

[32] H. Yan, X. Zhao, N. Guo, Z. Lyu, Y. Du, S. Xi, R. Guo, C. Chen, Z. Chen, W. Liu, C. Yao, J. Li, S.J. Pennycook, W. Chen, C. Su, C. Zhang, J. Lu, Atomic engineering of high-density isolated Co atoms on graphene with proximal-atom controlled reaction selectivity, *Nat. Commun.* 9 (2018) 3197.

[33] M. Zhu, L. Zhang, S. Liu, D. Wang, Y. Qin, Y. Chen, W. Dai, Y. Wang, Q. Xing, J. Zou, Degradation of 4-nitrophenol by electrocatalysis and advanced oxidation processes using Co_3O_4 @C anode coupled with simultaneous CO_2 reduction via SnO_2 /CC cathode, *Chin. Chem. Lett.* 31 (2020) 1961–1965.

[34] X. Zhao, C. Xiang, F. Zhang, F. Yao, R. Sheng, Q. Ding, W. Liu, H. Zhang, X. Zhou, Transformation from 3D boron organic polymers to 1D nanorod arrays: loading highly dispersed nanometal for green catalysis, *ACS Appl. Mater. Interfaces* 11 (2019) 43214–43222.

[35] H. Zhang, L. Wu, R. Feng, S. Wang, C.-S. Hsu, Y. Ni, A. Ahmad, C. Zhang, H. Wu, H.-M. Chen, W. Zhang, Y. Li, P. Liu, F. Song, Oxygen vacancies unfold the catalytic potential of NiFe-layered double hydroxides by promoting their electronic transport for oxygen evolution reaction, *ACS Catal.* 13 (2023) 6000–6012.

[36] K. Chu, Y. Luo, P. Shen, X. Li, Q. Li, Y. Guo, Unveiling the synergy of O-vacancy and heterostructure over MoO_{3-x} /MXene for N_2 electroreduction to NH_3 , *Adv. Energy Mater.* 12 (2022) 2103022.

[37] X. Dong, Z. Fang, Y. Gu, X. Zhou, C. Tian, Two-dimensional porous Cu–CuO nanosheets: Integration of heterojunction and morphology engineering to achieve high-effective and stable reduction of the aromatic nitro-compounds, *Chin. Chem. Lett.* 34 (2023), 107295.

[38] S. Oh, H. Yu, Y. Han, H.-S. Jeong, H.-J. Hong, 3-D porous cellulose nanofibril aerogels with a controllable copper nanoparticle loading as a highly efficient non-noble-metal catalyst for 4-nitrophenol reduction, *Chemosphere* 301 (2022), 134518.

[39] X. Li, Z. Lin, Q. Yuan, B. Sun, F. Chen, Z. Ma, T. Long, G. Li, M. Fu, A highly effective and reusable platinum nanoblock based on graphene/polyamino acid nanofilms for 4-nitrophenol degradation, *Appl. Surf. Sci.* 589 (2022), 153029.

[40] G. Kresse, D. Joubert, From ultrasoft pseudopotentials to the projector augmented-wave method, *Phys. Rev. B* 59 (1999) 1758–1775.

[41] H.J. Kulik, M. Cococcioni, D.A. Scherlis, N. Marzari, Density functional theory in transition-metal chemistry: a self-consistent Hubbard U approach, *Phys. Rev. Lett.* 97 (2006), 103001.

[42] L. Geng, Z. Lin, Z. Li, S. An, X. Zhang, Z. Liu, D.-S. Zhang, Y.-Z. Zhang, S. Gao, H. Han, Facile synthesis of holey lamellar CuO via ultrasonic chemical etching toward highly efficient hydrogenation of 4-nitrophenol under mild conditions, *J. Solid State Chem.* 292 (2020), 121698.

[43] X. Zhang, H. Wang, X. Jiang, H. Sun, Z. Qu, Study of synergistic effect between CuO and CeO₂ over CuO@CeO₂ core–shell nanocomposites for NH₃-SCO, *Catal. Sci. Technol.* 9 (2019) 2968–2981.

[44] C. Huang, W. Ye, Q. Liu, X. Qiu, Dispersed Cu₂O octahedrons on h-BN nanosheets for p-nitrophenol reduction, *ACS Appl. Mater. Interfaces* 6 (2014) 14469–14476.

[45] J. Hu, X. Zeng, G. Wang, B. Qian, Y. Liu, X. Hu, B. He, L. Zhang, X. Zhang, Modulating mesoporous Co_3O_4 hollow nanospheres with oxygen vacancies for highly efficient peroxyomonosulfate activation, *Chem. Eng. J.* 400 (2020), 125869.

[46] F. Cao, Y. Xiao, Z. Zhang, J. Li, Z. Xia, X. Hu, Y. Ma, Y. Qu, Influence of oxygen vacancies of CeO₂ on reverse water gas shift reaction, *J. Catal.* 414 (2022) 25–32.

[47] G. Ma, W. Tang, A. Wang, L. Zhang, J. Guan, N. Han, Y. Chen, Heterojunctioned CuO/Cu₂O catalyst for highly efficient ozone removal, *J. Environ. Sci.* 125 (2023) 340–348.

[48] G. Jing, L. Zhang, Y. Ma, J. Wu, Q. Wang, G. Wu, L. Yan, S. Zeng, Comparison of Au–Ce and Au–Cu interaction over Au/CeO₂–CuO catalysts for preferential CO oxidation, *CrystEngComm* 21 (2019) 363–371.

[49] L. Geng, M. Zhang, W. Zhang, M. Jia, W. Yan, G. Liu, Rational design of carbon support to prepare ultrafine iron oxide catalysts for air oxidation of alcohols, *Catal. Sci. Technol.* 5 (2015) 3097–3102.

[50] L. Geng, J. Song, B. Zheng, S. Wu, W. Zhang, M. Jia, G. Liu, Aerobic oxidative coupling of alcohols and amines to imines over iron catalysts supported on mesoporous carbon, *Chin. J. Catal.* 37 (2016) 1451–1460.

[51] J. Liang, Q. Song, J. Wu, Q. Lei, J. Li, W. Zhang, Z. Huang, T. Kang, H. Xu, P. Wang, X. Zhou, P.K. Wong, H. Li, X. Meng, Z. Jiang, C.-S. Lee, Anchoring copper single atoms on porous boron nitride nanofiber to boost selective reduction of nitroaromatics, *ACS Nano* 16 (2022) 4152–4161.

[52] N. Zhang, J. Wang, Q. Li, Y. Xin, L. Zheng, Y. Wang, Z. Zhang, Enhanced selective catalytic reduction of NO_x with NH₃ over homoatomic dinuclear sites in defective α -Fe₂O₃, *Chem. Eng. J.* 426 (2021), 131845.

[53] L. Geng, G. Li, X. Zhang, X. Wang, C. Li, Z. Liu, D.-S. Zhang, Y.-Z. Zhang, G. Wang, H. Han, Rational design of CuO/SiO₂ nanocatalyst with anchor structure and hydrophilic surface for efficient hydrogenation of nitrophenol, *J. Solid State Chem.* 296 (2021), 121960.

[54] L. Geng, J. Song, Y. Zhou, Y. Xie, J. Huang, W. Zhang, L. Peng, G. Liu, CeO₂ nanorods anchored on mesoporous carbon as an efficient catalyst for imine synthesis, *Chem. Commun.* 52 (2016) 13495–13498.

[55] H. Yi, Y. Wang, L. Diao, Y. Xin, C. Chai, D. Cui, D. Ma, Ultrasonic treatment enhances the formation of oxygen vacancies and trivalent manganese on α -MnO₂ surfaces: mechanism and application, *J. Colloid Interface Sci.* 626 (2022) 629–638.

[56] L. Geng, S. An, X. Wang, J. Chen, Z. Liu, X. Zhang, D.-S. Zhang, Y.-Z. Zhang, T. Wågberg, G. Hu, Valence-mixed CuO_x-nanoparticles anchored biomass-based carbon nanofiber for boosting toxic nitroarenes reduction: synthesis, kinetics, and mechanisms, *J. Environ. Chem. Eng.* 10 (2022), 108689.

[57] X. Wang, J. Zheng, P. Li, X.-B. Yin, S. Wang, B. Zhang, J. Xu, M. Zhang, Facile strategy for the synthesis of silver nanoparticles on magnetic Fe₃O₄@C core–shell nanocomposites and their application in catalytic reduction, *Dalton Trans.* 51 (2022) 3170–3179.

[58] F. Tong, X. Liang, F. Ma, X. Bao, Z. Wang, Y. Liu, P. Wang, H. Cheng, Y. Dai, B. Huang, Z. Zheng, Plasmon-mediated nitrobenzene hydrogenation with formate as the hydrogen donor studied at a single-particle level, *ACS Catal.* 11 (2021) 3801–3809.